THE JOURNAL OF PHYSICAL CHEMISTRY B

Article

pubs.acs.org/JPCB

Ionic Liquid Dynamics Measured with 2D IR and IR Pump–Probe Experiments on a Linear Anion and the Influence of Potassium Cations

Amr Tamimi and Michael D. Fayer*

Department of Chemistry Stanford University, Stanford, California 94305, United States

ABSTRACT: The room-temperature ionic liquid EmimNTf$_2$ (1-ethyl-3-methylimidazolium bis(trifluoromethylsulfonyl)imide) was studied with two-dimensional infrared (2D IR) spectroscopy and polarization selective pump–probe (PSPP) experiments using low-concentration selenocyanate ($SeCN^-$) as the vibrational probe. $SeCN^-$ was added as EmimSeCN, which keeps the cation the same. KSeCN was also used, so K^+ was added. Two 2D IR polarization configurations were employed: ⟨XXXX⟩ (all pulses have the same polarization) and ⟨XXYY⟩ (the first two pulse polarizations are perpendicular to that of the third pulse and the echo). The spectral diffusion differs for the two configurations, demonstrating that reorientation-induced spectral diffusion, in addition to structural spectral diffusion (SSD), plays a role in the observed dynamics. The SSD was extracted from the 2D IR time-dependent data. The samples with EmimSeCN have dynamics on several fast time scales; however, when KSeCN is used, both the PPSP anisotropy decay and the 2D IR decays have low amplitude offsets (nondecaying values at long times). The size of the offsets increased with increased K^+ concentration. These results are explained in terms of a two-ensemble model. A small fraction of the $SeCN^-$ is located in the regions modified by the presence of K^+, causing a substantial slowing of the $SeCN^-$ orientational relaxation and spectral diffusion. Having a small ensemble of $SeCN^-$ that undergoes very slow dynamics is sufficient to explain the offsets. For the major ensemble, the dynamics with and without K^+ are the same.

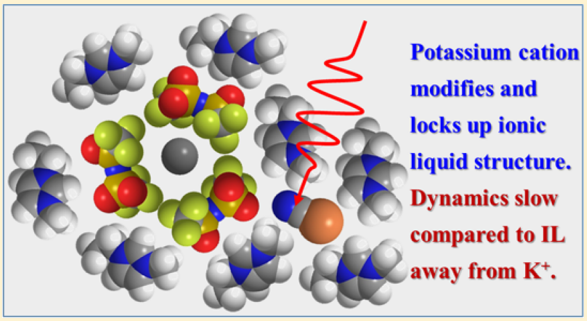

I. INTRODUCTION

Ionic liquids (ILs) have been the focus of extensive research owing to their extremely low vapor pressure,[1,2] ability to solvate disparate and challenging solutes,[3,4] and extensive variety and tunability.[3−5] ILs are defined as salts that are liquid below the boiling point of water. Room-temperature ionic liquids (RTILs) are ILs that are liquid around room temperature. The low melting point is typically achieved by using molecular ions, often organic, that are asymmetric, large, have diffuse or delocalized charge, or have some combination of these properties. The presence of these properties in the cation, anion, or both disfavors crystallization by reducing the enthalpic incentive or increasing the entropic cost.[2,3] The large number of possible candidates for such cations and anions gives rise to the aforementioned variety and tunability.[3−5]

The combination of unique IL properties renders them attractive for a large number of applications, with some having already found their way into practical use. A number of applications, such as their use as green solvents because of their low vapor pressure,[5] their use as native phase-transfer catalytic solvents,[6−8] or their use in battery electrolytes,[9−12] rely on tuning their solvation properties. Such a tuning process can be facilitated through a greater understanding of the microscopic details of the IL structure and dynamics.

A large number of studies have targeted the nanoscopic structure of ILs, which continues to be an area of active research and debate.[3,13−19] The techniques employed for structural determination, however, can only yield information about the solvation environment of a probe molecule insofar as the presence of the molecule does not alter its environment. Solvation, by necessity, involves appreciable interactions with the solvent. Moreover, the dynamics of the solute molecule are of intrinsic interest as well as being reporters on the structure of the local environment and its interactions with the solute. A practically useful probe of these interactions is the orientational and frequency dynamics (spectral diffusion) of a vibrational chromophore. Ultrafast infrared spectroscopic techniques can directly characterize the orientational and spectral dynamics of a molecular vibrational probe. Here we employ a small linear anion, namely, the selenocyanate ion ($SeCN^-$), as a vibrational probe of ILs.

An important class of RTILs consists of imidazolium cations with asymmetric alkyl substitutions on the nitrogens, paired with an array of anions.[2] The exact nature of the substitutions on the cation, as well as the choice of anion, influences the IL properties, which can be selected for a particular application. 1-

Special Issue: William M. Gelbart Festschrift

Received: January 13, 2016
Revised: February 12, 2016
Published: February 12, 2016

ACS Publications © 2016 American Chemical Society

DOI: 10.1021/acs.jpcb.6b00409
J. Phys. Chem. B 2016, 120, 5842−5854

Ethyl-3-methylimidazolium bis(trifluoromethylsulfonyl)imide ($EmimNTf_2$) has the combination of low viscosity, practical synthesis, and good chemical stability. In addition, the wide electrochemical window of stability may make $EmimNTf_2$ useful for battery applications.[20] Combined with its ready availability and extensive characterization, these factors make $EmimNTf_2$ a useful subject for this study.

Related work from this research group has focused on uncharged but hydrogen-bonding vibrational probes as a function of probe size,[21] a comparison between charged and uncharged fluorescent probes as a function of IL chain length,[22] and a study of the dependence of fluorescent probe dynamics and overall IL dynamics on lithium cation concentration.[23,24]

In this study, we characterize the dynamics, both spectral and orientational, of $SeCN^-$ in $EmimNTf_2$ and the influence of the addition of potassium cations on dynamics. To this end, $SeCN^-$ in $EmimNTf_2$ is studied using polarization selective two-dimensional infrared (2D IR) spectroscopy and polarization selective infrared pump−probe spectroscopy (PSPP). 2D IR characterizes the spectral diffusion of the vibrational probe, which reports on the structural fluctuations of the RTIL and the transience of solvation structures. The pump−probe experiments yield the vibrational lifetime and anisotropy decay of the probe. The latter characterizes the orientational dynamics of the $SeCN^-$ transition dipole vector. The orientational dynamics of the $SeCN^-$ are also necessary to extract the IL structural dynamics from the 2D IR experiments given the recent observations[25] and theoretical explication[25,26] of reorientation-induced spectral diffusion (RISD).

The approximation of independent spectral diffusion and orientational dynamics,[27−29] which is widely adopted, is observed to break down when significant orientational randomization occurs on a faster time scale than at least some component of the system structural dynamics.[25,26] RTILs have structural dynamics that occur over a wide range of times scales, and RISD has been previously observed in RTIL systems.[25]

The range of liquid structures causes a corresponding range of spectral shifts of the vibrational probe frequency, leading to an inhomogeneously broadened absorption line. Spectral diffusion refers to the randomization of the probe's vibrational frequency because of fluctuations of its environment and possible motions of the probe itself. Because $SeCN^-$ has a permanent dipole moment, the interactions causing these spectral shifts can occur via the first-order Stark effect.[30,31] The first-order Stark effect depends on the projection of the electric field along the probe ion's dipole moment. The evolving environment therefore influences the probe frequency through vector interactions between the probe and the electric field generated by the sample. For a relatively static electric field produced by a slowly evolving component of the RTIL's structure, reorientation of the vibrational probe changes the projection of the electric field along the dipole direction. The reorientation of the probe then modulates the resultant vibrational shifts, causing spectral diffusion.[25,26] Thus, both structural evolution of the liquid and reorientation of the probe can contribute to spectral diffusion

The RISD contribution to the polarization resolved 2D IR signal depends on the experiment's polarization configuration, that is, parallel (the three excitation pulses and the echo pulse have the same polarization ⟨XXXX⟩) or perpendicular (the first two excitation pulses' polarization are perpendicular to the third pulse and echo polarization ⟨XXYY⟩). For the parallel configuration, molecules will tend to be excited with the same polarization that gives rise to the signal. As they rotate, their frequencies will change, but they will also rotate into directions that contribute less to the signal. Therefore, the RISD will be somewhat mitigated by the reduction in the contribution of the reorienting molecules to the detected 2D IR signal. For the perpendicular configuration, molecules will be initially excited with their transition dipoles in directions that tend to be perpendicular to the signal polarization. As they rotate, their frequencies change and their transition dipoles will tend to move toward the readout polarization. Therefore, as rotation changes their frequency, they also contribute more to the 2D IR signal, amplifying their contribution to the observed spectral diffusion. The result is that RISD in ⟨XXYY⟩ makes a greater contribution, resulting in faster spectral diffusion than in ⟨XXXX⟩.[25,26] Using the recently developed RISD theory, the structural spectral diffusion (SSD) can be separated from the RISD. The RISD contribution to the total spectral diffusion is determined by the orientational relaxation of the probe molecules measured by the polarized pump−probe experiments. Therefore, there are no adjustable parameters in the RISD term used in the analysis of the total spectral diffusion.[25,26]

Recent 2D IR experiments in the parallel configuration addressed a vibrational probe (thiocyanate) similar to the one studied here in closely related ILs in an attempt to address the role of hydrogen bonding in determining the viscosity of ILs using the hydrogen bonding between the cation and the probe as a proxy for this mechanism.[32] A follow-up study examined the effect of adding water or introducing the potassium cation to the RTIL;[33] however, pump−probe experiments were not conducted and the total spectral diffusion dynamics were not separated into SSD and RISD contributions. An interesting result of the 2D IR thiocyanate experiments was the observation of an offset in the spectral diffusion decays only in the presence of a potassium counterion to the thiocyanate probe, as opposed to a native IL cation.[33] An offset is caused by a component of the spectral diffusion that is so slow that there is negligible decay in the experimental time window, which is limited by the vibrational lifetime. An offset when K^+ is present is also observed in this study using $SeCN^-$, where the longer CN stretch lifetime of $SeCN^-$ assists in characterizing the magnitude of the offset. Additionally, a K^+ concentration dependence of the offset was observed here. A set of control experiments was also performed with EmimSeCN, introducing the probe with a native IL cation, and no offset was observed. In addition, an offset in the orientational relaxation was found only when K^+ was present. These results are discussed in terms of a picture in which K^+ causes local structuring of the IL that is very slow to evolve. A small fraction of the $SeCN^-$ vibrational probes are located in these slowly evolving K^+ induced structures, giving rise to the offsets in the anisotropy and the SSD.

II. EXPERIMENTAL PROCEDURES AND DATA ANALYSIS

A. Sample Preparation. Three samples were used in this study. Two solutions are KSeCN dissolved in $EmimNTf_2$ and one was made with EmimSeCN dissolved in $EmimNTf_2$. KSeCN and $EmimNTf_2$ were purchased from commercial sources (Acros and Iolitec, respectively) and used after extended drying under vacuum and moderate heating (∼100 mTorr and ∼65 °C). The amount of water in the dried RTILs

DOI: 10.1021/acs.jpcb.6b00409
J. Phys. Chem. B 2016, 120, 5842−5854

was characterized by coulometric Karl Fischer titration (Mettler Toledo) and found to be under 10 ppm. EmimSeCN was prepared for these experiments from KSeCN and Emim iodide according to the synthesis of Wang et al.[34] After drying, the materials were stored in a nitrogen atmosphere glovebox. Solutions were prepared in the glovebox gravimetrically. KSeCN was added at molar ratios of 1:200 and 1:60 ion pairs per $EmimNTf_2$ and EmimSeCN was added with a mole ratio of 1:200.

The RTIL solutions are sandwiched between one inch diameter calcium fluoride windows with a polytetrafluoroethylene ring spacer to determine the sample path length. These sample cells are assembled in the glovebox then placed in the infrared spectrometry setup with an ambient temperature of 295 K. The spectrometer was purged with moisture-free air, which eliminates water vapor absorption lines in the laser.

Before and after the ultrafast infrared experiments were conducted, linear Fourier transform infrared (FT-IR) spectra of the samples were collected using a Nicolet 6700 FT-IR spectrometer to ensure that no appreciable sample decay had taken place and no water had been picked up during the experiments. For added consistency, the path length is varied between 100 and 250 μm across the different samples to maintain an absorbance of between 0.13 and 0.27. A one-time linear spectrum is also collected for an $EmimNTf_2$ sample, which was used for background subtraction in the linear FT-IR spectra.

B. Polarization Selective Pump−Probe Spectroscopy. Both PSPP and 2D IR measurements were performed with pump−probe geometry using the same optical platform. Details of the setup have been previously reported;[35] here a brief description is presented. A home-built mid-IR optical parametric amplifier, which was pumped by a Ti:sapphire regenerative amplifier, produced ∼170 fs pulses centered at 2075 cm^{-1} with ∼8 μJ pulse energy. The mid-IR pulses were split into a weaker probe pulse and a stronger pump pulse. The weak pulse was routed through a mechanical delay line, which was used to set the waiting time, T_w, for the 2D IR experiments (see later) and the delay time in the PSPP experiments. The strong pulse was sent to an acousto-optic mid-IR Fourier-domain pulse-shaper. The output beam from the pulse shaper, which generated pulses 1 and 2 in the 2D IR experiments and the single pump pulse in the PSPP experiments, was crossed in the sample with the probe pulse. The probe pulse, which carried the signal in pump−probe and vibrational echo experiments, was sent to a spectrometer equipped with a 32-element HgCdTe (MCT) IR array detector. In the 2D IR experiments, the pulse shaper was used to make two of the three excitation pulses (1 and 2) and control their delay and phase (phase cycling). In the PSPP experiments the pulse shaper was used to chop the pump pulse and for phase cycling. In both experiments, the phase cycling removes scattered light from the pump that can interfere with measurements of small signals in the probe direction.

The method for acquiring the polarization-selective pump−probe spectra was optimized to ensure that the parallel and perpendicular polarization configurations were acquired with the same experimental conditions. The probe polarization is fixed at horizontal (in the plane of the optical table), with an extra polarizer (wire-grid polarizer, ISP Optics) before the last mirror preceding the sample to eliminate any depolarization effects from the preceding optics and delay-line corner-cube. The pump-beam polarization is changed from horizontal to 45° relative to the probe using a half-wave-plate and polarizer. The polarizer was placed immediately before the sample to eliminate any depolarization. Directly after the sample, the probe is resolved using a polarizer mounted in an automated rotation stage, which alternates between +45 and −45° relative to the probe polarization. Because the pump polarization is +45°, these correspond to the parallel and perpendicular configurations, respectively. Because both pump and probe are never changed before the sample, the first three interactions have the same magnitude in both configurations. Moreover, in both configurations, the probe intensity is reduced by half, keeping the local oscillator intensities equal. Because the response of the spectrometer grating is polarization-dependent, another polarizer is placed right before the entrance slit and set to horizontal polarization. This reduces the intensity of both parallel and perpendicular signals, as well as the probe, by half, but guarantees unbiased detection of both polarization pathways.

The principal 2D IR data analysis did not rely on being able to add or subtract spectra from different polarization configurations. Signal-to-noise was, therefore, prioritized, and a different scheme for controlling the polarization was employed. The probe is kept horizontal as in the PSPP experiments, but instead of pumping at 45°, we pump at 0 and 90° for the ⟨XXXX⟩ and ⟨XXYY⟩ pathways, respectively. The resolving polarizer immediately after the sample is kept horizontal and is not changed. Because recovering isotropic spectra (discussed later) requires the ability to add spectra, comparison with the corresponding PSPP experiments was used to ensure the correct relative amplitudes.

Polarization-selective pump−probe spectroscopy measures the vibrational lifetime and the anisotropy, which is proportional to the second-order Legendre polynomial orientational correlation function, $C_2(t)$.[27] The form of this correlation function is known for diffusive orientational dynamics as well as for various restricted diffusion models (wobbling-in-a-cone).[36−39] The analysis of the anisotropy has been extensively employed in developing an understanding of the orientational dynamics of molecular probes.[21,40−42]

In measuring the anisotropy, two configurations where the pump and probe have parallel and perpendicular polarizations are acquired. For third-order pump−probe spectroscopy, the orientational contribution to any polarization configuration is given by the following equations, where the parallel and perpendicular acquired signals are $S_{\parallel}(t)$ and $S_{\perp}(t)$, respectively. The population lifetime decay is $P(t)$.[27]

$$S_{\parallel} = P(t)[1 + 0.8C_2(t)] \tag{1}$$

$$S_{\perp} = P(t)[1 - 0.4C_2(t)] \tag{2}$$

From these two experiment configurations, the following two observables can be extracted

$$P(t) = [S_{\parallel}(t) + 2S_{\perp}(t)]/3 \tag{3}$$

$$r(t) = \frac{S_{\parallel}(t) - S_{\perp}(t)}{S_{\parallel}(t) + 2S_{\perp}(t)} \tag{4}$$

where $r(t)$ is the anisotropy, defined as $r(t) = 0.4C_2(t)$.

For an anisotropy decay that is a single exponential, a common physical model is a single orientational diffusion process. An initial deviation from 0.4 at very short time is caused by the ultrafast inertial orientational motions.[41] The

DOI: 10.1021/acs.jpcb.6b00409
J. Phys. Chem. B 2016, 120, 5842−5854

inertial drop is too fast to measure; however, frequently the anisotropy decay is not a single exponential. A multiexponential can be described in terms of a hierarchy of diffusive processes, each limited to an angular cone with a certain half angle. The angular limitation is imposed by a local interaction. As the solvent structures randomize, the entire cone reorients on a slower time scale.

An orientational correlation function under restricted reorientation does not decay to zero but to a level determined by the extent of orientational space that remains unsampled. $C_2(t)$ decays to the square of an order parameter Q.[36,37] Explicitly including the wobbling in a cone model with a single cone

$$Q^2 = \left(\frac{1}{2}\cos\theta_0(1 + \cos\theta_0)\right)^2 \tag{5}$$

where θ_0 is the half angle of the cone.[36−39] Including the final complete diffusive orientational randomization yields[40]

$$C_2(t) = (Q^2 + (1 - Q^2)\exp(-t/\tau_c))\exp(-t/\tau_m) \tag{6}$$

where τ_c is the time constant for the restricted diffusion in the cone and τ_m is the time constant for the final complete orientational randomization.

Because the anisotropies measured here are triexponentials with an initial inertial drop, an inertial cone and two diffusive cones are included in addition to the final free diffusion. The resulting form for $C_2(t)$, which is used in fitting the anisotropy curves is[21]

$$\begin{aligned} C_2(t) = {} & (1 - T^2)\exp(-t/\tau_{in}) + T^2(1 - S^2)\exp(-t/\tau_{c1}) \\ & + T^2S^2(1 - R^2)\exp(-t(1/\tau_{c2} + 1/\tau_m)) \\ & + T^2S^2R^2\exp(-t/\tau_m) \end{aligned} \tag{7}$$

where T, S, and R are the order parameters for the inertial and two diffusive cones, respectively, and τ_{in}, the time constant for the inertial cone, is taken to be much faster than our time resolution. The size of the inertial cone thus reflects the initial value of the anisotropy when the experimental curve is extrapolated a few hundred femtoseconds back to $t = 0$.

C. 2D IR Spectroscopy. In a 2D IR experiment, three excitation pulses impinge on the sample with controllable time delays. The nonlinear interaction of the three pulses with the vibrational probe molecules ($SeCN^-$) generates a fourth pulse, the vibrational echo. The time between pulses 1 and 2 is τ, and the time between pulses 2 and 3 is T_w. The vibrational echo pulse is emitted after pulse 3.

The two pump pulses (1 and 2) label all of the vibrational oscillators with their initial frequencies. During the time period T_w, the frequencies of the vibrational oscillators evolve because of both SSD and RISD. Then, pulse 3 generates the vibrational echo signal that reads out the frequencies of the vibrational oscillators after the system has had the period T_w to evolve. The vibrational echo signal propagates collinearly with the pulse 3, which serves as the local oscillator (LO) to detect the phase of the echo signal.

The 2D IR spectra require two Fourier transforms to go from the time domain to the frequency domain. The spectrograph performs one of the Fourier transforms experimentally by resolving the echo/LO pulse into its composite frequencies giving the ω_m (vertical axis) of the 2D spectrum. The horizontal axis, ω_τ, is obtained by scanning τ. When τ is scanned, the echo moves in phase relative to the fixed LO, producing an interferogram. The interferogram, recorded at each ω_m, is numerically Fourier transformed to give the ω_τ axis of the 2D spectrum

For each T_w, τ is scanned and a 2D IR spectrum is obtained. The spectral diffusion (combined SSD and RISD) is extracted from the evolution of the 2D band shape at each T_w. At short T_w, the detection frequency (ω_m) is approximately the same as the excitation frequency (ω_τ), giving a spectrum that is elongated along the diagonal (upper right to lower left corners of the 2D spectrum). The shape of the spectrum becomes more symmetrical as spectral diffusion progresses, which causes the initial and final frequencies to be less correlated. The spectrum will be completely round when all structures have been sampled during the period T_w.

The results of the 2D IR experiments are analyzed in terms of the frequency−frequency correlation function (FFCF), which quantifies the spectral diffusion in terms of the frequency fluctuation amplitudes and time constants. The FFCF is the probability that a vibration with an initial frequency in the inhomogeneous spectral distribution still has the same frequency at a later time, averaged over all initial frequencies. To extract the FFCF from the 2D spectra, the center line slope (CLS) analysis was employed.[43,44] A fit to the CLS versus T_w curve, which is the normalized FFCF, gives spectral diffusion time constants and amplitude factors. The FFCF is described with a multiexponential model

$$C_{tot}(t) = \langle\delta\omega(t)\delta\omega(0)\rangle = \sum_i \Delta_i^2\exp(-t/\tau_i) \tag{8}$$

Here $\delta\omega(t) = \omega(t) - \langle\omega\rangle$ is the instantaneous frequency fluctuation with $\langle\omega\rangle$ the average frequency. Δ_i is the frequency fluctuation amplitude of each component, and τ_i is its associated time constant. A component of the FFCF with $\Delta_i\tau_i \ll 1$ is motionally narrowed. When a component is motionally narrowed, Δ and τ cannot be determined separately. The motionally narrowed homogeneous contribution to the absorption spectrum has a pure dephasing line width given by $\Gamma^* = \Delta^2\tau/\pi = 1/\pi T_2^*$, where T_2^* is the pure dephasing time. The observed homogeneous dephasing time, T_2, also has contributions from the vibrational lifetime and orientational relaxation

$$\frac{1}{T_2} = \frac{1}{T_2^*} + \frac{1}{2T_1} + \frac{1}{3T_{or}} \tag{9}$$

where T_2^*, T_1, and T_{or} are the pure dephasing time, vibrational lifetime, and orientational relaxation times, respectively. The total homogeneous line width is $\Gamma = 1/\pi T_2$. The total homogeneous dephasing time, T_2, and the values of Δ_i in units of frequency are obtained from the experimental data by a simultaneous fit to the CLS decay and the experimental linear absorption line shape.[43]

D. Reorientation-Induced Spectral Diffusion. As discussed in the Introduction, the total FFCF, $C_{tot}(t)$, can have contributions from both SSD and RISD. To assess the extent of the RISD contribution, one measures the FFCF using the CLS method in both the parallel ($\langle XXXX\rangle$) and perpendicular ($\langle XXYY\rangle$) 2D IR polarization configurations. If the CLS decays (normalized FFCFs) are identical to these two configurations, then there is no RISD. As shown in the 2D IR data later, the parallel and perpendicular CLS decays are different, and therefore RISD must be taken into account in

DOI: 10.1021/acs.jpcb.6b00409
J. Phys. Chem. B 2016, 120, 5842−5854

analyzing the data to extract the SSD, which reflects the structural evolution of the IL.

For first-order Stark effect coupling or any vector coupling that is first-order in the interaction that determines the probe frequency, the total FFCF, $C_{tot}(t)$, has been shown to have the form

$$C^{i}_{tot}(t) = F_{SSD}(t)R_{i}(t) \tag{10}$$

where $F_{SSD}(t)$ is the structural contribution to the FFCF, which is caused by fluctuations in the liquid structure and $R_i(t)$ is the RISD contribution, where i is parallel, perpendicular, or isotropic (see later).[25,26] The second term, $R_i(t)$, captures the effect of probe dipole reorientation on the spectral fluctuations including polarization weighting to account for the experimental geometry. The normalized RISD contribution has been calculated to be for the parallel case

$$R_{para}(t) = \frac{3}{25}\left[\frac{11C_1(t) + 4C_3(t)}{1 + 0.8C_2(t)}\right] \tag{11}$$

and for the perpendicular case

$$R_{perp}(t) = \frac{3}{25}\left[\frac{7C_1(t) - 2C_3(t)}{1 - 0.4C_2(t)}\right] \tag{12}$$

where $C_1(t)$, $C_2(t)$, and $C_3(t)$ are the first-, second-, and third-order Legendre polynomial orientational correlation functions, respectively.[25,26] It is important to point out that there are no adjustable parameters in eqs 11 and 12. $C_2(t)$ is measured using the PPSP experiments. Once $C_2(t)$ is known from the experiments, $C_1(t)$ and $C_3(t)$ are obtained from relations previously derived that relate them to $C_2(t)$.[26] The relations include the wobbling-in-a-cone and the complete final diffusive randomization.

In the experiments, $C^{para}_{tot}(t) = F_{SSD}(t)R_{para}(t)$ and $C^{perp}_{tot}(t) = F_{SSD}(t)R_{perp}(t)$ are measured. The two T_w-dependent CLS decay curves are fit simultaneously. The adjustable parameters are in the structural part of the FFCF, $F_{SSD}(t)$. $F_{SSD}(t)$ is the same in the parallel and perpendicular 2D IR data. While $C^{para}_{tot}(t)$ and $C^{perp}_{tot}(t)$ are the direct experimental observables, there is another quantity that is useful. Simulations of 2D IR data, in general, do not include polarized radiation fields. Simulations calculate $C^{iso}_{tot}(t)$, where iso stands for isotropic.

$$C^{iso}_{tot}(t) = F_{SSD}(t)R_{iso}(t) \tag{13}$$

where $R_{iso}(t) = C_1(t)$.[25] As discussed later, $C^{iso}_{tot}(t)$ is obtained by adding the parallel 2D IR spectrum to twice the perpendicular 2D IR spectrum with the proper scaling at each T_w. The CLS method is then used on the resulting added spectra to obtain the normalized isotropic FFCF. It is important to note that the isotropic FFCF still has contributions from reorientation, RISD, and from SSD. $F_{SSD}(t)$ is the same in the parallel, perpendicular, and isotropic FFCFs.

III. RESULTS AND DISCUSSION

A. Linear Infrared Spectra. The linear FT-IR spectra of the CN stretch of $SeCN^-$ for the samples studied are shown in Figure 1. The spectra are identical to within experimental error and centered at 2063.7 cm^{-1}. The spectra are very slightly asymmetric, but this may be caused by a small error in baseline subtraction. A second possibility is that there is a small degree of the non-Condon effect in which the transition dipole is slightly larger on the red side of the line. A more significant

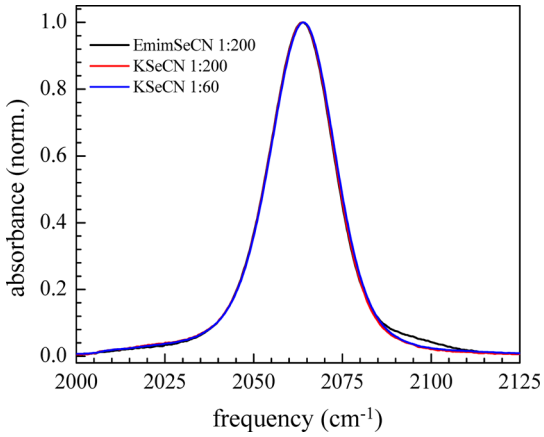

Figure 1. Background-subtracted FT-IR spectra of the CN stretch of $SeCN^-$ in three samples of $EmimNTf_2$. The $SeCN^-$ was added as EmimSeCN (mole ratio 1:200) or as KSeCN in mole ratios of 1:200 and 1:60. Within experimental error, the spectra are the same.

asymmetry has been observed for $SeCN^-$ in D_2O, which was shown to be caused by the non-Condon effect.[45] The possibility of a non-Condon effect will be discussed further later in connection with the lifetime data. Despite the very small asymmetry, the line shape is fit well with a single Voigt function. The full width at half-maximum (fwhm) is 22.0 ± 0.1 cm^{-1} for all three samples, and the Gaussian component of the Voigt is about twice the Lorenztian component.

It is interesting to note that the CN stretch of $SeCN^-$ is centered at 2075 cm^{-1} in D_2O, indicating strong hydrogen bonding, and at 2065 cm^{-1} in very small AOT reverse micelles, in which the $SeCN^-$ is interacting with the ionic head groups of the reverse micelles.[45] The fwhm in the IL is significantly narrower at 22 cm^{-1} compared with 35 cm^{-1} in D_2O. It is, however, broader than in the very small AOT reverse micelle (w_0 = 1), where the fwhm is 16 cm^{-1}. The similarity in peak position between the small reverse micelles and the IL is reasonable because the $SeCN^-$ is expected to predominantly interact with ions in both these environments. The narrower line width in the AOT reverse micelle can be understood as a smaller range of chemical environments, consistent with the micelles being relatively uniformly sized self-assembled systems, which therefore do not have as wide a range of environments as are possible in a room-temperature liquid.

B. Time-Resolved Measurements. *1. EmimSeCN in $EmimNTf_2$: PSPP.* The PSPP curves are processed in accordance with eqs 3 and 4 to yield the isotropic decay curve $P(t)$ and the anisotropy $r(t)$. $P(t)$ is the excited-state lifetime in the absence of other effects. A very small difference in the early portion of $P(t)$ was observed as a function of wavelength. If the $P(t)$ is fit with a single exponential, the result is a lifetime of 109 ps; however, the fit can be improved by assuming the absorption line is not uniformly pumped and that the fast components of the spectral diffusion, discussed later, bring the population across the line into equilibrium with the spectral diffusion time constants.[21,45] Using a triexponential fit with the first two components fixed at the spectral diffusion time constants yields an essentially perfect fit with a vibrational lifetime of 105 ps. The effect is therefore small.

There are two possible reasons why the spectral band is not uniformly pumped. The first is the non-Condon effect,[21,45,46] previously mentioned in connection with the line shape. The second is that the laser is not tuned to the exact center of the

DOI: 10.1021/acs.jpcb.6b00409
J. Phys. Chem. B 2016, 120, 5842−5854

absorption and there is a relatively large sloping absorption background. The result would be nonuniform pumping of the line even in the absence of the non-Condon effect. Both possibilities would result in nonexponential decays caused by spectral diffusion. We cannot distinguish these two possibilities, but a more substantial early time nonexponential decay for $SeCN^-$ in D_2O was shown to be caused by the non-Condon effect.[21] Regardless of the mechanism, the effect is small and does not influence any of the data analysis presented later. In the anisotropy decay, the experimental $P(t)$ is used in the denominator of eq 4 and removes $P(t)$ from the orientational relaxation regardless of its functional form.

We find no discernible wavelength dependence for the anisotropy in the vicinity of line center. This is in contrast with the observed wavelength dependence for hydroxyl probes in the same IL.[21] Figure 2 shows the anisotropy decay curve for

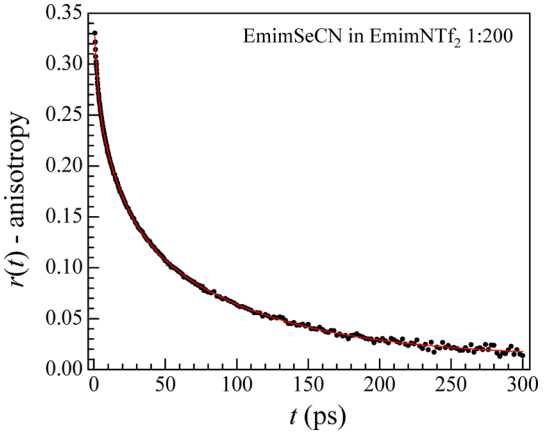

Figure 2. Anisotropy decay (orientational relaxation) of $SeCN^-$ in EmimSeCN (black points) and the triexponential fit to the data (red solid curve).

$SeCN^-$ in the sample of EmimSeCN in $EmimNTf_2$ at a 1:200 mol ratio. This curve is the average of eight wavelengths ranging from 2061 to 2070 cm^{-1}. The curve fits well to a triexponential with an initial inertial drop (the difference between 0.4 and the observed anisotropy at $t = 0$). The parameters that result from the triexponential fit are used with the triexponential form of eq 7 to extract the three cone angles (inertial, first diffusive, second diffusive) and the three decay times (first cone diffusion, second cone diffusion, and the final complete diffusive randomization). The errors from the fits are also propagated in this procedure. We will refer to this analysis as the "wobbling analysis" for brevity. The resulting cone parameters are summarized in Table 1.

We note at this point that very slight errors in normalization between the parallel and perpendicular measurements are sometimes unavoidable due to experimental limitations. Because these errors, when small, look predominantly like a small offset with no other effect on the time dependence, a free offset term was added to the triexponential fit to account for any such errors. The offset is ~0.01 out of 0.4. Because the longest time component is ~90 ps and the data quality is excellent up to 300 ps, we can confidently extract the longtime component despite this additional degree of freedom. In addition to being able to verify that the resulting offset in the fit is small enough that the rest of the data is not compromised, the inclusion of this term in the fit ensures consistency with the other samples discussed later that contain K^+, which display real offsets of physical origin.

The cone angles and diffusion constants are broadly reflective of the classes of restrictions for angular displacement and the time scales on which these restrictions are relaxed or overcome. The most straightforward to interpret are the inertial cone and the final complete diffusive randomization. The inertial cone angle gives some insight into how much "room" a molecule has to reorient through ballistic motion. The value for $SeCN^-$ in $EmimNTf_2$, at 17°, is just smaller than the ranges reported for water, methanol, or ethanol in the same IL,[21] which at the center of their respective absorption lines have values in the low 20° range. The $SeCN^-$ value is also slightly smaller than the inertial cone angle for CO_2 in $EmimNTf_2$ (to be published), which is ~21°, but the error bars are large enough to overlap with the $SeCN^-$ value. Therefore, water and the alcohols, in which the hydroxyl moieties can form hydrogen bonds, have somewhat greater freedom to move ballistically than the probes $SeCN^-$ and CO_2. The hydrogen-bonding molecules are more restricted (smaller cone angle) at the redder wavelengths where hydrogen bonding is stronger.[21] Because the inertial cone for CO_2, a nonpolar probe, is not dramatically different in the IL from that of $SeCN^-$ and large rearrangements of the IL are unlikely to happen on a time scale fast enough to affect the inertial drop, we reason that the main restriction on ballistic motion in the IL is the available space in the native IL packing. In contrast, $SeCN^-$ was previously studied in D_2O, where the observed inertial drop is significantly larger.[45]

While the short time orientational relaxation involves restricted wobbling motions, the slowest time constant, τ_m, is the time constant for complete orientational relaxation. We can address the question as to whether the final complete orientational randomization is hydrodynamic. The diffusion constant under slip boundary conditions can be calculated from Debye–Stokes–Einstein (DSE)[47−49] theory using the formula

$$D = \frac{kT}{\eta V_{\text{eff}} \lambda} \tag{14}$$

where η is the viscosity (which we measured to be 39.3 cP at 295.4 K) and λ is a unitless parameter, tabulated as a function of the axis ratio.[50]

An electronic structure calculation of $SeCN^-$ with geometry optimization was run using the Gaussian09 package with a 6-311++G(3df,3pd) basis set and second order Møller–Plesset perturbation theory (MP2).[51] The resulting calculation was analyzed to obtain both bond lengths and a total MP2 density surface with a 0.002 isovalue, commonly found to give a good estimate for the van der Waals interaction surface.[52] The bond

Table 1. Wobbling-in-a-Cone Analysis for EmimSeCN in $EmimNTf_2$

θ_{in} (deg)	θ_{w1} (deg)	θ_{w2} (deg)	θ_{tot} (deg)	$t_1 = \tau_{c1}$ (ps)	t_2 (ps)	τ_{c2} (ps)	$t_3 = \tau_m$ (ps)
17.5 ± 0.8	22.9 ± 0.4	33.0 ± 0.4	42.9 ± 0.4	1.9 ± 0.1	15 ± 1	18 ± 1	88 ± 3

[a] θ represents inertial, wobbling, and total cone angles, t representes fit time constants, and τ represents time constants from the wobbling analysis for the corresponding cones and final complete orientational randomization.

DOI: 10.1021/acs.jpcb.6b00409
J. Phys. Chem. B 2016, 120, 5842−5854

length was used with published van der Waals radii for the atoms to calculate major and minor spheroidal axis lengths as a check. Lower and upper bounds for the minor axis can be calculated by using the radius near the CN bond or at the Se atom, respectively. The first is estimated by averaging the radii for C and N, and the latter is available as the Se van der Waals radius, 1.625 and 1.9 Å, respectively. Corresponding measurements were obtained using the density surface with reasonable agreement (1.761 and 2.2 Å). The major axis can be calculated by adding the bond lengths for this linear molecule with the radii for Se and N and dividing the resulting number by 2 to yield a radius. This number for the major axis is again in reasonable agreement with half the length of the density isosurface (3.22 and 3.29 Å, respectively). These numbers are used to calculate a ratio of the axes and an effective spheroidal volume, V_{eff}. The diffusion constant under slip boundary conditions was then calculated with eq 14.

The resulting C_2 diffusive time constant, $\tau = 1/(6D)$, using upper and lower bound values for the minor axis, are 96 and 126 ps, respectively, using tabulated van der Waals radii. The corresponding numbers using the MP2 total density isosurface are 74 and 122 ps. The agreement with the measured free diffusion time of 88 ± 3 ps indicates that $SeCN^-$ does reorient with slip boundary conditions, meaning that the barrier to reorientation is the necessity of displacing the surrounding solvent. In the specific context of the IL, we reason that the linear probe cannot reorient completely without some rearrangement of the surrounding ions and that for a molecule of this size and shape factor the IL rearrangement is the major restriction on free diffusion.

The first diffusive cone angle for $SeCN^-$ is 23°, a value intermediate between ethanol (~13°) and carbon dioxide (32°). Because this value shows the greatest variation of the orientational parameters across the three probes (hydrogen bonding, charged, uncharged), it stands to reason that it is significantly influenced by the nature of the interaction between the probe and the IL.

The second diffusive cone shows a similar trend as the free diffusion in that ethanol (30°) more strongly resembles $SeCN^-$ (33°) and CO_2 (36°) than smaller hydrogen bonding solutes that exhibit smaller cone angles.[53] Selenocyanate is again an intermediate case between the hydrogen-bonding ethanol and nonpolar solute CO_2. The differences in the cone angles, while not large, may suggest a role of specific interactions between the solute and its IL environment; however, the overall similarity among these small solutes suggests that the local IL structure surrounding them is dominant in determining the constraints on orientational relaxation that lead to the wobbling cones.

2. EmimSeCN in EmimNTf$_2$: 2D IR. As discussed in the Introduction and in connection with eqs 10−12, the FFCF obtained from the 2D IR measurements of spectral diffusion can have two contributions, which are the time-dependent structural fluctuation of the IL medium and RISD. If RISD contributes to the FFCF, then the CLS decays measured in the parallel and perpendicular polarization configurations will differ. In the main portion of Figure 3 are CLS decays for the parallel, ⟨XXXX⟩, and perpendicular, ⟨XXYY⟩, polarization configurations. The significant difference in the decays shows that RISD contributes to the total FFCF (see eq 10). Therefore, the data will be analyzed to separate the FFCF into its SSD and orientational spectral diffusion components.

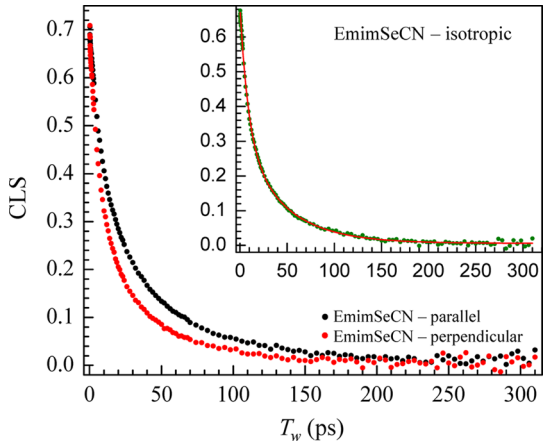

Figure 3. 2D IR spectral diffusion dynamics in the form of the CLS decay (normalized FFCF). The main portion of the data shows decays in the parallel and perpendicular polarization configurations. The fact that they are different shows that reorientation-induced spectral diffusion (RISD) in addition to structural spectral diffusion (SSD) contributes to the FFCF. The inset shows the isotropic decay that is derived from the parallel and perpendicular 2D IR spectrum. This decay has contributions from RISD. It is the decay that is most readily compared with a full MD simulation of the 2D IR measured FFCF.

As discussed in connection with eq 13, the parallel and perpendicular decays are not readily amenable to simulation, but the isotropic decay is. The isotropic CLS is the nonpolarization weighted FFCF. This CLS is obtained by analyzing isotropic 2D IR spectra in the same fashion as the other two configurations. The isotropic spectrum at each T_w is obtained by adding the parallel 2D spectrum to twice the perpendicular 2D spectrum, but the parallel and perpendicular spectra must have the correct relative amplitudes. We obtain the correct relative amplitudes using the projection slice theorem, which says the projection of the 2D spectrum onto the ω_m axis is the same as the pump−probe spectrum.[54] The parallel and perpendicular pump−probe spectra used to obtain the $P(t)$ and $r(t)$ have the correct relative amplitudes. So the projected parallel and perpendicular 2D spectra are scaled to match the corresponding pump−probe spectra.

The inset in Figure 3 shows the isotropic CLS (normalized FFCF). This is the total FFCF, as given in eq 13. The solid curve through the data is a biexponential fit to the decay. The fit is improved slightly by allowing a small offset. The offset is 0.006. The offset may be caused by experimental error or it may be real as discussed in the following sections. The biexponential fit parameters are $A_1 = 0.37$, $\tau_1 = 8.9$ ps, $A_2 = 0.31$, and $\tau_2 = 44.8$ ps, where the A_1 and A_2 are amplitudes and τ_1 and τ_2 are time constants. Because a full simulation would include both the SSD and the RISD, it should be compared with the values given above or the values for the full FFCF for the isotropic decay given in Table 2, which are obtained from the CLS fit values and the linear absorption spectrum.[43] This latter analysis yields the homogeneous dephasing time, $T_2 = 1.51$ ps, and the corresponding homogeneous line width, $\Gamma = 7$ cm^{-1}. From eq 9, the homogeneous line width has contributions from pure dephasing (ultrafast fluctuations that are motionally narrowed), the vibrational lifetime, and the orientational relaxation time. The lifetime and the orientational relaxation make only very small contributions, so the homogeneous line width is dominated by pure dephasing.

DOI: 10.1021/acs.jpcb.6b00409
J. Phys. Chem. B 2016, 120, 5842−5854

Table 2. FFCF Parameters (eq 8) for EmimSeCN in EmimNTf$_2$ at 1:200 from the Fit Shown in the Inset of Figure 3[a,b]

T_2 (ps)	Γ (cm^{-1})	Δ_1 (cm^{-1})	τ_1 (ps)	Δ_2 (cm^{-1})	τ_2 (ps)	Δ_{off} (cm^{-1})
1.51 ± 0.02	7.0 ± 0.1	5.9 ± 0.1	8.9 ± 0.5	5.6 ± 3	44.8 ± 2	0.76 ± 0.1

[a] T_2, homogeneous dephasing time; Γ, homogeneous line width, fwhm; τ_i, ith component decay constant; Δ_i, ith component inhomogeneous width, standard deviation; [b] The total inhomogeneous width (standard deviation) is the square root of the sum of the squares of the Δs. The fwhm is this value multiplied by 2.35, which is 19.2 cm^{-1}. Without the offset, the value is 19.1 cm^{-1}; the offset is negligible. The total line shape is the total inhomogeneous Gaussian component convolved with Γ, the homogeneous Lorentzian component.

The model for the polarization weighted FFCF (eqs 10−12) attributes the spectral fluctuations to a first-order Stark shift mechanism. For molecules with a permanent dipole moment, the use of the first order Stark mechanism has worked well in reproducing 2D IR data in a variety of simulations.[30,55−62] In addition, the RISD mechanism assumes that reorientation of the small probe does not by itself produce structural changes in the IL. These two assumptions yield the analytical form for the polarization-weighted FFCFs detailed in eqs 10−12. The parallel and perpendicular CLS data are fit to these analytical forms. The RISD terms in eqs 11 and 12 have no adjustable parameters.[26] Therefore, the data are fit by adjusting the parameters in the SSD portion of the FFCF. The structural component of the FFCF is modeled as a multiexponential.

The fits to the data are shown in Figure 4. The main portion of the Figure displays the parallel and perpendicular data (points) and the fits (solid curves). The inset shows the isotropic curve (points) and the fit (solid curve). The isotropic curve falls between the parallel and perpendicular curves. For clarity it is displayed in the inset. The SSD factor, $F_{SSD}(t)$, describes only the structural fluctuations of the IL, which are modeled as the magnitude and direction of the electric field the vibrational probe experiences. $F_{SSD}(t)$ is independent of the polarization configuration of the experiment (parallel, perpendicular, or isotropic) because it is independent of the reorientation of the vibrational probe. For this reason, $F_{SSD}(t)$ is held to be the same in fitting all three CLS curves simultaneously. Using a multiexponential form for the SSD, we find that a biexponential with a small offset gives the best description of the data. Adding an exponential with a starting time constant faster than our first exponential yields an unphysical negative amplitude. On the other hand, adding an exponential slower than our second exponential either converges to our second exponential when an offset is permitted or diverges to infinity when the offset is fixed to zero, which in effect produces an offset. While the offset itself is not strictly needed, it improves the quality of the fit in accounting for the lack of convergence between the parallel and perpendicular polarizations within our resolved time window.

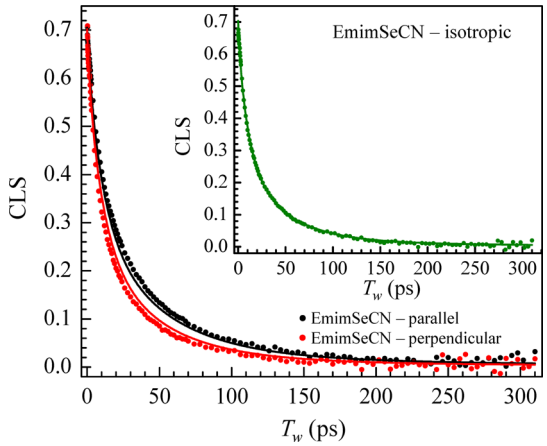

Figure 4. 2D IR data for the CN stretch of SeCN$^-$ in EmimNTf$_2$ for the parallel, perpendicular, and isotropic (inset) CLS decays (points) and simultaneous fits to the data (solid curves) using the RISD theory that includes the effects of both structural spectral diffusion and reorientation-induced spectral diffusion.

Before discussing the values obtained from the simultaneous fits to the three curves, we would like to comment on the quality of the fits. While the fit line goes right through the isotropic CLS points, the parallel and perpendicular fit curves are not quite on top of the corresponding data. The fit curves correctly capture the short and long time convergence of the curves and, critically, reproduce the correct trend for intermediate times. What is not captured is the full extent of the difference between parallel and perpendicular, which is slightly larger in the experimental data than in the fits. As discussed later, the errors in the fits produce very little difference in the F_{SSD} values.

Two reasons present themselves as possible explanations for the discrepancy between the data and the fits. The first possibility is additional broadening, which is not entirely explained by first-order Stark-effect-induced shifts. Adding a scalar term to the $F_{SSD}(t)$ cannot reproduce the observed effect; however, there could be an additional vector coupling term that is not accounted for, a second-order Stark effect contribution, for example. Because SeCN$^-$ has a strong permanent dipole, it is unlikely that there is a significant second-order contribution.

The second possibility is the presence of correlation between the electric-field fluctuations in the pocket containing the vibrational probe and the reorientation of the probe. Full

Table 3. SSD Parameters for Simultaneous and Independent RISD Fits to Parallel, Perpendicular, and Isotropic CLS Curves for EmimSeCN in EmimNTf$_2$[a]

data sets fit	A_1	τ_1	A_2	τ_2	A_{off}
simultaneous para, perp, iso	0.35 ± 0.03	11 ± 1	0.36 ± 0.03	54 ± 5	0.025 ± 0.005
simultaneous para, perp, no iso	0.34 ± 0.04	11 ± 1	0.37 ± 0.04	51 ± 6	0.028 ± 0.006
parallel only	0.32 ± 0.03	12 ± 1	0.39 ± 0.03	52 ± 4	0.032 ± 0.004
perpendicular only	0.38 ± 0.03	10 ± 1	0.34 ± 0.03	50 ± 5	0.021 ± 0.005
isotropic only	0.38 ± 0.03	13 ± 1	0.33 ± 0.03	61 ± 7	0.015 ± 0.006

[a] A_1 and A_2 are the amplitudes of the two exponentials and A_{off} is the offset amplitude. τ_1 and τ_2 are the time constants of the two exponentials.

DOI: 10.1021/acs.jpcb.6b00409
J. Phys. Chem. B 2016, 120, 5842−5854

reorientation of the probe cannot occur without some solvent motions. It is possible that these solvent motions result in a change in the electric field that the probe experiences. Because the probe is small, the extent of the IL rearrangement necessary is not large and the impact of the resulting correlation is most likely minor.

To determine the extent of the error in the fits given that they do not reproduce the parallel and perpendicular curves perfectly when the three data sets (parallel, perpendicular and isotropic) are fit simultaneously, we did several different types of fits to determine how much the parameters varied. We fit all three curves simultaneously, which are the fits shown in Figure 4. We fit only the parallel and perpendicular curves simultaneously, and we fit each curve individually. The results of the fits are collected in Table 3. Within the error bars, all of the fits give the same results. The simultaneous fit to all three curves yields $\tau_1 = 11 \pm 1$ ps and $\tau_2 = 54 \pm 5$ ps, which are the same values as the average of the values found from all five fits given in Table 3. The consistency of the various fits indicates that the results are meaningful. The SSD amplitudes are split fairly evenly between an 11 ps component and a 54 ps components.

Fluctuations in the solvent structure will result in electric-field fluctuations felt by our probe and give rise to the SSD. While it is not possible to identify the nature of the motions leading to these time scales without simulations, the numbers themselves somewhat constrain the possible range of motions. We expect motions such as solvent orientational wobbling and small packing or density changes to contribute to these two time scales. The time for complete orientational randomization of $EmimNTf_2$ is 380 ps, as measured using optical heterodyne-detected optical Kerr effect experiments. The slowest SSD time constant, 54 ps, is significantly faster than the time for complete orientational randomization of the liquid. Therefore, orientational randomization of the liquid is not required to sample all liquid structures that give rise to the $SeCN^-$ probe's inhomogeneously broadened absorption line. The fast spectral diffusion of the probe compared with the bulk reorientation time suggests that the inhomogeneous broadening involves relatively local IL structures in the vicinity of the probe rather than the global configuration of the liquid. Then, the motions that cause spectral diffusion are those that randomize these more or less local configurations.

3. KSeCN in $EmimNTf_2$: PSPP and 2D IR. As mentioned in the Introduction, recent 2D IR experiments on thiocyanate in an IL found that when K^+ was present, the FFCF displayed a long time offset.[33] Here we expand consideration of the influence of potassium cations on the structure and dynamics in $EmimNTf_2$. By combining anisotropy measurements with 2D IR measurements we can gain a better understanding of the nature of the influence of K^+. In addition $SeCN^-$ has a vibrational lifetime that is substantially longer than that of SCN^-, which makes examination of a long time offset more useful.

Two concentrations of KSeCN in $EmimNTf_2$ were prepared: a 1:60 mol ratio and a 1:200 mol ratio. Figure 5 shows the anisotropy decays of three samples of selenocyanate in $EmimNTf_2$ with and without K^+. One curve is the same, as shown in Figure 2, for which the selenocyanate was added in the form of EmimSeCN with a mole ratio of 1:200. There is no K^+ in that sample. In the other two samples, KSeCN was added to $EmimNTf_2$ in mole rations of 1:200 and 1:60. All three curves appear the same at short time; however, at long times

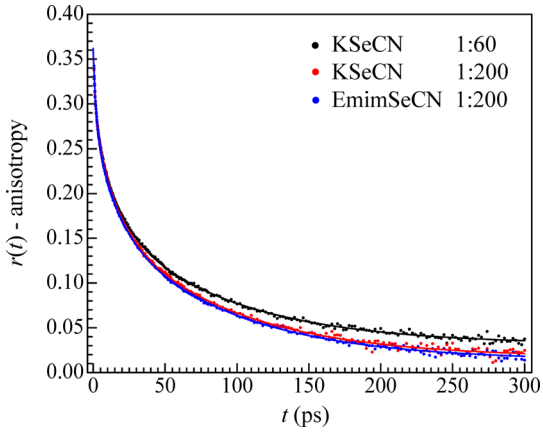

Figure 5. Anisotropy decays of $SeCN^-$ (points) and fits (solid curves) for three $EmimNTf_2$ samples with the $SeCN^-$ added as EmimSeCN (mole ratio 1:200) or as KSeCN in mole ratios of 1:200 and 1:60. As the K^+ concentration increases, a long time offset increases; otherwise, the reorientation dynamics are the same in the three samples.

the curves diverge. The difference among the curves is the size of a long time offset; that is, the data do not decay to zero in the time window of the experiments, which is limited by the vibrational lifetime. Table 4 shows the results of the triexponential fits. Only the time constants are reported. The cone angles are the same as those reported for the EmimSeCN sample (no potassium) in Table 1. From Table 4 it is clear that the major difference is the offset value, y_0. The time constants are the same within experimental error. If a global fit is performed on the three curves, in which the time constants are shared but the offsets are independent, the resulting curves through each data set fit the data essentially perfectly with an *R*-squared value of 0.999. With the global fit, the time constants are $t_1 = 1.75$, $t_2 = 14.4$, and $t_3 = 84.3$.

Table 4. Fitting Results to the Anisotropy Decays Shown in Figure 4

sample	t_1 (ps)	t_2 (ps)	t_3 (ps)	y_0[a]
EmimSeCN 1:200	1.9 ± 0.2	15 ± 1	88 ± 3	0.012 ± 0.001
KSeCN 1:200	1.8 ± 0.2	15 ± 1	86 ± 3	0.016 ± 0.001
KSeCN 1:60	1.5 ± 0.2	13 ± 2	79 ± 4	0.033 ± 0.001

[a] y_0, offset

The addition of K^+ increases the offset but does not change the major part of the orientational relaxation. For the 1:60 sample the offset has become quite large. The addition of the K^+, a small spherical cation, which is quite different from $Emim^+$, generates the offset. The smallest offset is observed for the sample in which EminSeCN was added rather than KSeCN. The preparation of the EmimSeCN required ion exchange. Mass spectrometry of the material showed that it contained small amounts of Ag^+ and I^- ions. The presence of these ions in the no K^+ sample is likely responsible for the offset. The addition of 1:200 K^+ produces a somewhat larger offset, while the 1:60 K^+ sample has a very substantial offset. A concentration-dependent offset grows with potassium concentration.

A complementary picture can be drawn by analyzing the effect of potassium concentration on the 2D IR CLS data. Figure 6 shows the parallel and perpendicular CLS curves for the 1:60 potassium-containing sample with the 1:200

DOI: 10.1021/acs.jpcb.6b00409
J. Phys. Chem. B 2016, 120, 5842−5854

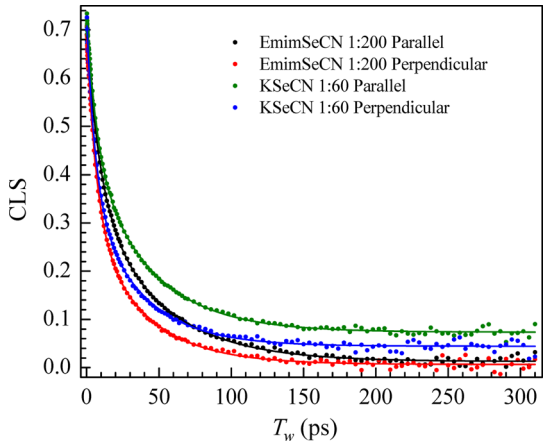

Figure 6. 2D IR CLS data (points) for the CN stretch of $SeCN^-$ in $EmimNTf_2$ for the parallel and perpendicular polarization configurations and fits (solid curves) for two samples with KSeCN added in mole ratios of 1:200 and 1:60. When the K^+ concentration is increased the long time scale offset increases but otherwise dynamics remain the same.

EmimSeCN sample (no K^+) for comparison. The difference among the data sets is more striking than in the anisotropy data. While the no K^+ sample has a small offset, both polarizations of the 1:60 K^+ sample acquire significant offsets with the effect more pronounced for the parallel polarization. The parallel CLS curves for the three samples are displayed in Figure 7 to show clearly the effect of the addition of potassium.

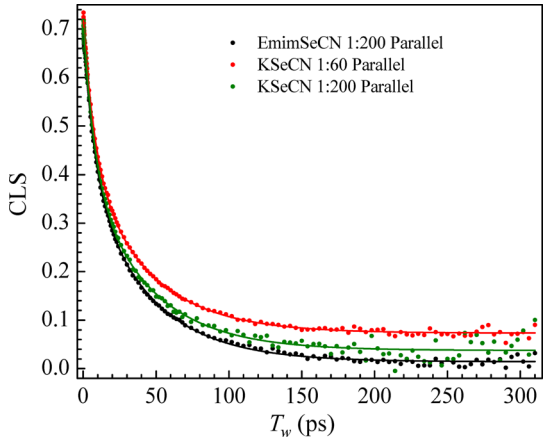

Figure 7. 2D IR data for the CN stretch of $SeCN^-$ in $EmimNTf_2$ (points) for the parallel polarization configuration only for three samples with the $SeCN^-$ added as EmimSeCN (mole ratio 1:200) or as KSeCN in mole ratios of 1:200 and 1:60. The Figure shows the increase in the long time offset as the K^+ concentration is increased. Other than the change in offset, the dynamics are the same.

To gauge the magnitude of the effect, we fit the parallel and perpendicular polarizations for the three samples to biexponentials with an offset. The parallel curves and the perpendicular curves can be fit just as well with shared time constants across the three samples. As in the anisotropy data, the time decays do not change with K^+ concentration. Only the size of the offset changes. Given that the offsets are barely affected by the choice of fitting procedure, we have displayed the results of the fits with shared time constants in Figure 7 to highlight the quality of the constrained fit. The resulting offsets are tabulated in Table 5. Going from no potassium to the two potassium-containing samples, the offset increases by a factor of

Table 5. Offsets from 2D IR CLS Data

sample	parallel offset	perpendicular offset
EmimSeCN 1:200	0.014 ± 0.001	0.007 ± 0.001
KSeCN 1:200	0.038 ± 0.001	0.020 ± 0.001
KSeCN 1:60	0.073 ± 0.001	0.044 ± 0.001

~3 and ~5 for the parallel polarization and ~2 and ~6 for the perpendicular polarization for the lower and higher concentration potassium containing samples. These numbers are not meant to be quantitative given the apparent sensitivity of the offset to impurities and the sensitivity of the later T_w points to scatter, particularly for the parallel polarization.

Performing the RISD analysis previously used but including additional offsets in the fits as independent parameters shows that, aside from the sample dependent offset, the three samples have the same SSD time dependence within experimental error. Therefore, for both the anisotropy decays and the 2D IR CLS decays, the observable dynamics are essentially the same, independent of the K^+ concentration. In addition, the FT-IR spectra shown in Figure 1 do not depend on the K^+ concentration.

The anisotropy offsets, which increase with K^+ concentration, mean that there is orientational relaxation that is extremely slow, too slow to measure in the experimental time window. The CLS offsets demonstrate that there is spectral diffusion that is exceedingly slow, again too slow to measure the decay time. There is a physical model that explains the effects of K^+ on the observables. The $SeCN^-$ vibrational probes exist in two distinct structural environments. Most of the vibrational probes are not influenced by the presence of K^+. They are located in the IL in sites where the structure and dynamics of the liquid are the same as pure $EmimNTf_2$. This subensemble of environments yields the same spectrum, the same orientational relaxation, and the same spectral diffusion whether or not K^+ is present in the sample.

There is a second subensemble. The IL in proximity of K^+ has a structure distinct from the bulk of the IL. Both simulations[63] and experimental data[24,63] indicate that adding Li^+ to ILs similar to $EmimNTf_2$ causes local structuring about the lithium cation. There are also experimental results showing that Na^+ can also induce local structuring.[64,65] While K^+ is larger than Li^+ and Na^+, it is still a spherical cation ion with a large positive charge density compared with $Emim^+$. Like Li^+, it is reasonable to assume that the solvation around K^+ produces a local IL structure that is very different than that of the bulk liquid. A small fraction of the $SeCN^-$ vibrational probes will be located in these regions. The vibrational anisotropy offset then arises from $SeCN^-$ in these K^+-modified volumes because in these regions the $SeCN^-$ ions have much slower orientational relaxation then they do in the bulk liquid. In this picture, the K^+ organized regions have a tighter structure that evolves more slowly than the bulk liquid and slows orientational relaxation. Increasing the K^+ concentration from 1:200 to 1:60, increases the fraction of $SeCN^-$ ions that are in the K^+ organized regions, so the anisotropy offset increases (see Figure 5 and Table 4).

The K^+ structured regions have two effects on the 2D IR CLS decays (see Figures 6 and 7 and Table 5). First, the proposed more slowly evolving environments around the vibrational probe will slow down the spectral diffusion and give

DOI: 10.1021/acs.jpcb.6b00409
J. Phys. Chem. B 2016, 120, 5842−5854

rise to the offset that we observe. As with the anisotropy, the size of the offset increases with K^+ concentration, which is consistent with a larger fraction of the vibrational probes being located in the K^+ modified regions. The second effect involves the RISD. If the SSD had slowed, but the anisotropy decay had not slowed, RISD would have caused the CLS to decay to zero (no offset) despite the slow SSD. To have an offset in the CLS requires both the SSD and the anisotropy decay to become very slow.

The proposed two-ensemble model, in which K^+ produces structurally distinct regions that have much slower dynamics than the bulk $EmimNTf_2$, accounts for all of the observables. Even for the 1:60 K^+ mole ratio, the fraction of the volume that is structurally distinct will not be large. The result is that the absorption spectrum is not changed, and the observed anisotropy decays and CLS decays are not changed by the addition of K^+; however, the vibrational probes that are in the K^+-modified regions experience much slower structural change, giving rise to the offsets in both the anisotropy decays and the CLS decays. In the sample with no K^+, that is, $EmimNTf_2$ with EmimSeCN added for the vibrational probe, one would expect no offsets; however, a small offset is seen in the anisotropy decay (Figure 5) and in the CLS decays (Figures 6 and 7). As previously discussed, the method of preparation of EmimSeCN from EmimI[34] resulted in low concentrations of Ag^+ and I^- ions remaining in the material. The presence of these ions can also cause local restructuring of the IL, which produces slowly evolving structures that give rise to the offsets.

IV. CONCLUDING REMARKS

Understanding solvation structure and dynamics in ILs continues to be a challenge. Solvation is important because it is intimately tied to the same properties that make ILs different from common solvents. Ionic solutes have strong interactions with the surrounding solvent ions. The importance of understanding solvation in ILs, in general, and for ionic solutes, specifically, derives both from the fundamental insights obtained about the local structure of ILs as well as from the importance of solvation and its ramifications on applications of ILs such as their use as battery electrolytes. To this end, we have investigated $SeCN^-$, which is used as a vibrational probe, in one of the most common ILs, $EmimNTf_2$. Three samples of $EmimNTf_2$ were studied with the $SeCN^-$ introduced as EmimSeCN (mole ratio 1:200) or as KSeCN in mole ratios of 1:200 and 1:60. Linear FT-IR spectra of the CN stretch of $SeCN^-$ in the three samples are essentially identical (see Figure 1). PSPP and 2D IR spectroscopies were used to examine the liquid dynamics and structure without and with K^+ in the samples.

Orientational relaxation measurements of the $SeCN^-$ yielded multiexponential decays that were analyzed using the wobbling-in-a-cone model and diffusive final complete orientational randomization. The 2D IR experiments, conducted with parallel and perpendicular polarization configurations, gave different decays of the frequency-frequency correlation function. These results show that in addition to SSD there are contributions to the FFCF from RISD.[25,26] Using the results from the orientational relaxation measurements, the contribution from RISD was separated out, and the SSD contribution to the FFCF was obtained.

The observables derived from these time-resolved experiments characterized the structural fluctuations of the IL reported by the vibrational probe in the form of reorientation and the spectral fluctuations as interactions change and the IL structure evolves. The orientational data revealed the ability of the ionic solute to undergo ballistic motion, to be constrained by and then to break free of local interactions, and finally to completely randomize its orientation. The diffusive orientational randomization was found to be consistent with slip boundary conditions and a local viscosity seen by the probe equal to the bulk viscosity. The structural dynamics measured by the analysis that yielded the SSD occurred on the 11 and 54 ps time scales. These are the time scales for sampling the structural variations in the IL that give rise to the inhomogeneous broadening of the absorption spectrum.

When the samples contained K^+, an additional component in the dynamics was observed. While in all three samples, the orientational dynamics and the spectral diffusion within the experimental time window were the same, the samples with K^+ also had a small long time scale offset in both the orientational relaxation and the spectral diffusion. The size of the offsets increased when the K^+ concentration was increased. An offset means that there are very slow dynamics that are too slow to measure within the time window limited by the probe's vibrational lifetime. A two-ensemble model was presented to explain the K^+-induced offsets. The majority of the $SeCN^-$ vibrational probes are not influenced by the K^+, and this ensemble gives rise to the fast dynamics that are independent of the presence of K^+. It was proposed that K^+ produces local structuring of the IL that is distinct from the bulk of the liquid. These K^+ structured volumes have much slower dynamics than the bulk of the liquid. The small fraction of the $SeCN^-$ vibrational probes that are in these slowly evolving structured regions have much slower dynamics and give rise to the offsets. The size of the offsets increases with K^+ concentration as a larger fraction of the $SeCN^-$ is located in the K^+ structured regions.

The experiments presented here provide detailed insights into the nature of the dynamics, structure, and interactions of an ionic solute in a RTIL. Future experiments will look for the offset effect with ions, both cations and anions, other than K^+. Comparisons of the size of the offsets at the same concentrations for different ions may provide information on the relative size of the small ion-induced structured regions.

AUTHOR INFORMATION

Corresponding Author

*E-mail: fayer@stanford.edu.

Notes

The authors declare no competing financial interest.

ACKNOWLEDGMENTS

We thank Patrick L. Kramer, Jun Nishida, and Chiara H. Giammanco for helpful discussions. We also thank Heather Bailey at the Stanford University Chemistry department for conducting the OKE measurements. This work was funded by the Division of Chemical Sciences, Geosciences, and Biosciences, Office of Basic Energy Sciences of the U.S. Department of Energy through Grant DE-FG03-84ER13251 and the Air Force Office of Scientific Research Grant FA9550-16-1-0104.

REFERENCES

(1) Ueno, K.; Tokuda, H.; Watanabe, M. Ionicity in Ionic Liquids: Correlation with Ionic Structure and Physicochemical Properties. *Phys. Chem. Chem. Phys.* **2010**, *12*, 1649−1658.

DOI: 10.1021/acs.jpcb.6b00409
J. Phys. Chem. B 2016, 120, 5842−5854

(2) Castner, E. W.; Margulis, C. J.; Maroncelli, M.; Wishart, J. F. Ionic Liquids: Structure and Photochemical Reactions. *Annu. Rev. Phys. Chem.* **2011**, *62*, 85−105.
(3) Hayes, R.; Warr, G. G.; Atkin, R. Structure and Nanostructure in Ionic Liquids. *Chem. Rev.* **2015**, *115*, 6357−6426.
(4) Smiglak, M.; Metlen, A.; Rogers, R. D. The Second Evolution of Ionic Liquids: From Solvents and Separations to Advanced Materials—Energetic Examples from the Ionic Liquid Cookbook. *Acc. Chem. Res.* **2007**, *40*, 1182−1192.
(5) Plechkova, N. V.; Seddon, K. R. Applications of Ionic Liquids in the Chemical Industry. *Chem. Soc. Rev.* **2008**, *37*, 123−150.
(6) Bender, J.; Jepkens, D.; Hüsken, H. Ionic Liquids as Phase-Transfer Catalysts: Etherification Reaction of 1-Octanol with 1-Chlorobutane. *Org. Process Res. Dev.* **2010**, *14*, 716−721.
(7) Kumar, V.; Jamie Talisman, I.; Bukhari, O.; Razzaghy, J.; Malhotra, S. V. Dual Role of Ionic Liquids as Phase Transfer Catalyst and Solvent for Glycosidation Reactions. *RSC Adv.* **2011**, *1*, 1721−1727.
(8) Welton, T. Ionic Liquids in Catalysis. *Coord. Chem. Rev.* **2004**, *248*, 2459−2477.
(9) Lewandowski, A.; Świderska-Mocek, A. Ionic Liquids as Electrolytes for Li-Ion Batteries—an Overview of Electrochemical Studies. *J. Power Sources* **2009**, *194*, 601−609.
(10) Kar, M.; Simons, T. J.; Forsyth, M.; MacFarlane, D. R. Ionic Liquid Electrolytes as a Platform for Rechargeable Metal-Air Batteries: A Perspective. *Phys. Chem. Chem. Phys.* **2014**, *16*, 18658−18674.
(11) Elia, G. A.; Hassoun, J.; Kwak, W. J.; Sun, Y. K.; Scrosati, B.; Mueller, F.; Bresser, D.; Passerini, S.; Oberhumer, P.; Tsiouvaras, N.; Reiter, J. An Advanced Lithium−Air Battery Exploiting an Ionic Liquid-Based Electrolyte. *Nano Lett.* **2014**, *14*, 6572−6577.
(12) Lin, M.-C.; Gong, M.; Lu, B.; Wu, Y.; Wang, D.-Y.; Guan, M.; Angell, M.; Chen, C.; Yang, J.; Hwang, B.-J.; Dai, H. An Ultrafast Rechargeable Aluminium-Ion Battery. *Nature* **2015**, *520*, 324−328.
(13) Del Pópolo, M. G.; Voth, G. A. On the Structure and Dynamics of Ionic Liquids. *J. Phys. Chem. B* **2004**, *108*, 1744−1752.
(14) Wang, Y.; Jiang, W.; Yan, T.; Voth, G. A. Understanding Ionic Liquids through Atomistic and Coarse-Grained Molecular Dynamics Simulations. *Acc. Chem. Res.* **2007**, *40*, 1193−1199.
(15) Canongia Lopes, J. N. A.; Pádua, A. A. H. Nanostructural Organization in Ionic Liquids. *J. Phys. Chem. B* **2006**, *110*, 3330−3335.
(16) Triolo, A.; Russina, O.; Bleif, H.-J.; Di Cola, E. Nanoscale Segregation in Room Temperature Ionic Liquids. *J. Phys. Chem. B* **2007**, *111*, 4641−4644.
(17) Triolo, A.; Russina, O.; Fazio, B.; Triolo, R.; Di Cola, E. Morphology of 1-Alkyl-3-Methylimidazolium Hexafluorophosphate Room Temperature Ionic Liquids. *Chem. Phys. Lett.* **2008**, *457*, 362−365.
(18) Russina, O.; Triolo, A.; Gontrani, L.; Caminiti, R.; Xiao, D.; Hines, L. G., Jr.; Bartsch, R. A.; Quitevis, E. L.; Plechkova, N. V.; Seddon, K. R. Morphology and Intermolecular Dynamics of 1-Alkyl-3-Methylimidazolium Bis{(Trifluoromethane)Sulfonyl}Amide Ionic Liquids: Structural and Dynamic Evidence of Nanoscale Segregation. *J. Phys.: Condens. Matter* **2009**, *21*, 424121.
(19) Hardacre, C.; Holbrey, J. D.; Mullan, C. L.; Youngs, T. G. A.; Bowron, D. T. Small Angle Neutron Scattering from 1-Alkyl-3-Methylimidazolium Hexafluorophosphate Ionic Liquids ($[C_n mim][PF_6]$, n = 4, 6, and 8). *J. Chem. Phys.* **2010**, *133*, 074510.
(20) Kim, J.-K.; Shin, C.-R.; Ahn, J.-H.; Matic, A.; Jacobsson, P. Highly Porous $LiMnPO_4$ in Combination with an Ionic Liquid-Based Polymer Gel Electrolyte for Lithium Batteries. *Electrochem. Commun.* **2011**, *13*, 1105−1108.
(21) Kramer, P. L.; Giammanco, C. H.; Fayer, M. D. Dynamics of Water, Methanol, and Ethanol in a Room Temperature Ionic Liquid. *J. Chem. Phys.* **2015**, *142*, 212408.
(22) Fruchey, K.; Fayer, M. D. Dynamics in Organic Ionic Liquids in Distinct Regions Using Charged and Uncharged Orientational Relaxation Probes. *J. Phys. Chem. B* **2010**, *114*, 2840−2845.
(23) Lawler, C.; Fayer, M. D. The Influence of Lithium Cations on Dynamics and Structure of Room Temperature Ionic Liquids. *J. Phys. Chem. B* **2013**, *117*, 9768−9774.
(24) Nicolau, B. G.; Sturlaugson, A.; Fruchey, K.; Ribeiro, M. C. C.; Fayer, M. D. Room Temperature Ionic Liquid-Lithium Salt Mixtures: Optical Kerr Effect Dynamical Measurements. *J. Phys. Chem. B* **2010**, *114*, 8350−8356.
(25) Kramer, P. L.; Nishida, J.; Giammanco, C. H.; Tamimi, A.; Fayer, M. D. Observation and Theory of Reorientation-Induced Spectral Diffusion in Polarization-Selective 2D IR Spectroscopy. *J. Chem. Phys.* **2015**, *142*, 184505.
(26) Kramer, P. L.; Nishida, J.; Fayer, M. D. Separation of Experimental 2D IR Frequency-Frequency Correlation Functions into Structural and Reorientation-Induced Contributions. *J. Chem. Phys.* **2015**, *143*, 124505.
(27) Tokmakoff, A. Orientational Correlation Functions and Polarization Selectivity for Nonlinear Spectroscopy of Isotropic Media. 1. Third Order. *J. Chem. Phys.* **1996**, *105*, 1−12.
(28) Tokmakoff, A.; Fayer, M. D. Homogeneous Vibrational Dynamics and Inhomogeneous Broadening in Glass-Forming Liquids: Infrared Photon Echo Experiments from Room Temperature to 10 K. *J. Chem. Phys.* **1995**, *103*, 2810−2826.
(29) Mukamel, S. *Principles of Nonlinear Optical Spectroscopy*; Oxford University Press: New York, 1995.
(30) Fried, S. D.; Bagchi, S.; Boxer, S. G. Measuring Electrostatic Fields in Both Hydrogen-Bonding and Non-Hydrogen-Bonding Environments Using Carbonyl Vibrational Probes. *J. Am. Chem. Soc.* **2013**, *135*, 11181−11192.
(31) Fried, S. D.; Wang, L.-P.; Boxer, S. G.; Ren, P.; Pande, V. S. Calculations of the Electric Fields in Liquid Solutions. *J. Phys. Chem. B* **2013**, *117*, 16236−16248.
(32) Ren, Z.; Ivanova, A. S.; Couchot-Vore, D.; Garrett-Roe, S. Ultrafast Structure and Dynamics in Ionic Liquids: 2D-IR Spectroscopy Probes the Molecular Origin of Viscosity. *J. Phys. Chem. Lett.* **2014**, *5*, 1541−1546.
(33) Ren, Z.; Brinzer, T.; Dutta, S.; Garrett-Roe, S. Thiocyanate as a Local Probe of Ultrafast Structure and Dynamics in Imidazolium-Based Ionic Liquids: Water-Induced Heterogeneity and Cation-Induced Ion Pairing. *J. Phys. Chem. B* **2015**, *119*, 4699−4712.
(34) Wang, P.; Zakeeruddin, S. M.; Moser, J.-E.; Humphry-Baker, R.; Grätzel, M. A Solvent-Free, SecCN-/$(SeCN)_3$- Based Ionic Liquid Electrolyte for High-Efficiency Dye-Sensitized Nanocrystalline Solar Cells. *J. Am. Chem. Soc.* **2004**, *126*, 7164−7165.
(35) Karthick Kumar, S. K.; Tamimi, A.; Fayer, M. D. Comparisons of 2D IR Measured Spectral Diffusion in Rotating Frames Using Pulse Shaping and in the Stationary Frame Using the Standard Method. *J. Chem. Phys.* **2012**, *137*, 184201.
(36) Kinosita, K.; Kawato, S.; Ikegami, A. Theory of Fluorescence Polarization Decay in Membranes. *Biophys. J.* **1977**, *20*, 289−305.
(37) Kinosita, K.; Ikegami, A.; Kawato, S. On the Wobbling-in-Cone Analysis of Fluorescence Anisotropy Decay. *Biophys. J.* **1982**, *37*, 461−464.
(38) Lipari, G.; Szabo, A. Effect of Librational Motion on Fluorescence Depolarization and Nuclear Magnetic-Resonance Relaxation in Macromolecules and Membranes. *Biophys. J.* **1980**, *30*, 489−506.
(39) Lipari, G.; Szabo, A. Model-Free Approach to the Interpretation of Nuclear Magnetic-Resonance Relaxation in Macromolecules 0.1. Theory and Range of Validity. *J. Am. Chem. Soc.* **1982**, *104*, 4546−4559.
(40) Tan, H.-S.; Piletic, I. R.; Fayer, M. D. Orientational Dynamics of Water Confined on a Nanometer Length Scale in Reverse Micelles. *J. Chem. Phys.* **2005**, *122*, 174501.
(41) Moilanen, D. E.; Fenn, E. E.; Lin, Y. S.; Skinner, J. L.; Bagchi, B.; Fayer, M. D. Water Inertial Reorientation: Hydrogen Bond Strength and the Angular Potential. *Proc. Natl. Acad. Sci. U. S. A.* **2008**, *105*, 5295−5300.
(42) Fenn, E. E.; Wong, D. B.; Fayer, M. D. Water Dynamics in Small Reverse Micelles in Two Solvents: Two-Dimensional Infrared

DOI: 10.1021/acs.jpcb.6b00409
J. Phys. Chem. B 2016, 120, 5842−5854

Vibrational Echoes with Two-Dimensional Background Subtraction. *J. Chem. Phys.* **2011**, *134*, 054512.
(43) Kwak, K.; Park, S.; Finkelstein, I. J.; Fayer, M. D. Frequency-Frequency Correlation Functions and Apodization in 2D-IR Vibrational Echo Spectroscopy, a New Approach. *J. Chem. Phys.* **2007**, *127*, 124503.
(44) Kwak, K.; Rosenfeld, D. E.; Fayer, M. D. Taking Apart the Two-Dimensional Infrared Vibrational Echo Spectra: More Information and Elimination of Distortions. *J. Chem. Phys.* **2008**, *128*, 204505.
(45) Yuan, R.; Yan, C.; Tamimi, A.; Fayer, M. D. Molecular Anion Hydrogen Bonding Dynamics in Aqueous Solution. *J. Phys. Chem. B* **2015**, *119*, 13407−13415.
(46) Schmidt, J. R.; Corcelli, S. A.; Skinner, J. L. Pronounced Non-Condon Effects in the Ultrafast Infrared Spectroscopy of Water. *J. Chem. Phys.* **2005**, *123*, 044513.
(47) Moog, R. S.; Ediger, M. D.; Boxer, S. G.; Fayer, M. D. Viscosity Dependence of the Rotational Reorientation of Rhodamine B in Mono- and Polyalcohol. Picosecond Transient Grating Experiments. *J. Phys. Chem.* **1982**, *86*, 4694−4700.
(48) Youngren, G. K.; Acrivos, A. Rotational Friction Coefficients for Ellipsoids and Chemical Molecules with the Slip Boundary Condition. *J. Chem. Phys.* **1975**, *63*, 3846−3849.
(49) Hu, C.-M.; Zwanzig, R. Rotational Friction Coefficients for Spheroids with the Slipping Boundary Condition. *J. Chem. Phys.* **1974**, *60*, 4354−4357.
(50) Sension, R. J.; Hochstrasser, R. M. Comment On: Rotational Friction Coefficients for Ellipsoids and Chemical Molecules with Slip Boundary Conditions. *J. Chem. Phys.* **1993**, *98*, 2490−2490.
(51) Frisch, M. J.; et al. *Gaussian 09*, revision D.01; Gaussian, Inc.: 2009.
(52) Doucet, J.-P.; Weber, J. 10 - Derivation and Visualization of Molecular Properties. In *Computer-Aided Molecular Design*; Weber, J.-P. D., Ed.; Academic Press: London, 1996; pp 301−327.
(53) Giammanco, C. H.; Kramer, P. L.; Yamada, S. A.; Nishida, J.; Tamimi, A.; Fayer, M. D. Coupling of Carbon Dioxide Stretch and Bend Vibrations Reveals Thermal Population Dynamics in an Ionic Liquid. *J. Phys. Chem. B* **2016**, *120*, 549−556.
(54) Gallagher Faeder, S. M.; Jonas, D. M. Two-Dimensional Electronic Correlation and Relaxation Spectra: Theory and Model Calculations. *J. Phys. Chem. A* **1999**, *103*, 10489−10505.
(55) Williams, R. B.; Loring, R. F.; Fayer, M. D. Vibrational Dephasing of Carbonmonoxy Myoglobin. *J. Phys. Chem. B* **2001**, *105*, 4068−4071.
(56) Geissler, P. L. Water Interfaces, Solvation, and Spectroscopy. *Annu. Rev. Phys. Chem.* **2013**, *64*, 317−337.
(57) Bagchi, S.; Boxer, S. G.; Fayer, M. D. Ribonuclease S Dynamics Measured Using a Nitrile Label with 2D IR Vibrational Echo Spectroscopy. *J. Phys. Chem. B* **2012**, *116*, 4034−4042.
(58) Bagchi, S.; Fried, S. D.; Boxer, S. G. A Solvatochromic Model Calibrates Nitriles' Vibrational Frequencies to Electrostatic Fields. *J. Am. Chem. Soc.* **2012**, *134*, 10373−10376.
(59) Terranova, Z. L.; Corcelli, S. A. Molecular Dynamics Investigation of the Vibrational Spectroscopy of Isolated Water in an Ionic Liquid. *J. Phys. Chem. B* **2014**, *118*, 8264−8272.
(60) Corcelli, S.; Skinner, J. L. Infrared and Raman Line Shapes of Dilute HOD in Liquid H_2O and D_2O from 10 to 90 °C. *J. Phys. Chem. A* **2005**, *109*, 6154−6165.
(61) Corcelli, S.; Lawrence, C. P.; Skinner, J. L. Combined Electronic Structure/Molecular Dynamics Approach for Ultrafast Infrared Spectroscopy of Dilute HOD in Liquid H_2O and D_2O. *J. Chem. Phys.* **2004**, *120*, 8107−8117.
(62) Lawrence, C. P.; Skinner, J. L. Vibrational Spectroscopy of Hod in Liquid D_2O. III. Spectral Diffusion, and Hydrogen-Bonding and Rotational Dynamics. *J. Chem. Phys.* **2003**, *118*, 264−272.
(63) Monteiro, M. J.; Bazito, F. F. C.; Siqueira, L. J. A.; Ribeiro, M. C. C.; Torresi, R. M. Transport Coefficients, Raman Spectroscopy, and Computer Simulation of Lithium Salt Solutions in an Ionic Liquid. *J. Phys. Chem. B* **2008**, *112*, 2102−2109.
(64) Wilkes, J. S. *Room Temperature Molten Salts for Advanced Energy Conversion and Storage*; DTIC Document: 1994.
(65) Tucker, T. G.; Angell, C. A. Approaches to, and Problems with, Ionic Liquid Electrolytes for Alkali Metal Electrochemical Devices: The Case of Low-Melting Chloroaluminate Binary Solutions. *J. Electrochem. Soc.* **2014**, *161*, H796−H801.

DOI: 10.1021/acs.jpcb.6b00409
J. Phys. Chem. B 2016, 120, 5842−5854